

Dark matter implications from the XENONnT and LZ data

Haipeng An,^{1,2,*} Fei Gao,^{1,2,†} Jia Liu,^{3,4,‡} Minghao Liu,^{5,1,§} Haoming Nie,^{1,2,¶} and Changlong Xu^{1,2,**}

¹*Department of Physics, Tsinghua University, Beijing 100084, China*

²*Center for High Energy Physics, Tsinghua University, Beijing 100084, China*

³*School of Physics and State Key Laboratory of Nuclear Physics and Technology, Peking University, Beijing 100871, China*

⁴*Center for High Energy Physics, Peking University, Beijing 100871, China*

⁵*Physics Department, Columbia University, New York, NY 10027, USA*

We investigate a possible dark matter origin of the high-energy nuclear-recoil excess reported by recent liquid xenon experiments, including XENONnT and LZ, which cannot be explained by standard elastic spin-independent WIMP scattering. Using our unified DIAMX framework, built on openly available data and likelihood models, we perform the first combined profile-likelihood fits to multiple WIMP-search datasets with a total exposure of $7.3 \text{ tonne} \times \text{year}$. We investigate that two broad classes of dark matter nucleon interactions, with velocity-dependent cross-section or inelastic (endo- and exothermic) scattering, can reproduce the observed high-energy recoil spectrum, reaching local significances up to 4σ . We further quantify the impact of ^{124}Xe double electron capture (DEC) backgrounds, finding that variations in the poorly known DEC charge yields can shift the inferred significances from below 1σ to 4σ . We point out that extending the same analysis to XENONnT and LZ data with recoil energies up to 300 keV, once available, will provide a powerful test of the dark matter interpretation, since the ^{124}Xe DEC background is expected to be negligible in this high-energy range.

Introduction Dark matter (DM) accounts for approximately one-fourth of the universe's total energy density today, yet its particle nature remains enigmatic. While various alternative models have been proposed, the weakly interacting massive particle (WIMP) remains the most compelling paradigm for DM due to its theoretical elegance and natural ability to explain the observed relic abundance through thermal freeze-out [1, 2]. Experiments investigating the direct interaction between WIMPs and Standard Model particles have produced stringent limits on the elastic spin-independent WIMP-nucleon cross section. Among them, experiments searching for nuclear recoil (NR) signals in liquid xenon (LXe) time projection chambers (TPC) are leading for DM masses ranging from a few GeV to tens of TeV [3–7], thanks to their sensitivity to low-energy events, low background levels, and excellent discrimination power between the dominant electronic recoil (ER) background and the NR signal.

Although no convincing evidence of WIMP-nucleus elastic scattering has been found, various experiments based on LXeTPC have independently found an excess in the nuclear recoil band at energies higher than 20 keV. The XENON1T collaboration observed 14 events in the NR signal reference region with a background expectation of 7.36 ± 0.61 with an exposure of $1.0 \text{ tonne} \times \text{year}$ [8]. In 2024, the PandaX-4T experiment released a WIMP search result based on a $1.53 \text{ tonne} \times \text{year}$ exposure, and observed 24 events ($20.5^{+2.5}_{-2.2}$ background events) in the NR reference region, a significant fraction of which have NR energies above 20 keV [7]. In this work, we examine the WIMP search datasets released by the XENONnT [5, 6] and LUX-ZEPLIN (LZ) [3, 4] experiments, with exposures of 3.1 and $4.2 \text{ tonne} \times \text{year}$, respectively. These two experiments are chosen because their exposures are large, and the models are relatively easy to construct, thanks to their

data and software availability. We select NR-like events in XENONnT and LZ and plot their energy spectrum in Fig. 1. An excess of NR-like events above $20 \text{ keV}_{\text{NR}}$ is present both in LZ and XENONnT data, and the spin-independent WIMP-nucleus elastic scattering model cannot explain it because of its exponentially-dropping spectrum shape.

The LZ collaboration interpreted the excess as the two-neutrino double electron capture ($2\nu\text{ECEC}$, or DEC) of ^{124}Xe background events leaking into the NR region, because they generate less charge than previously understood [4]. However, the exact charge yield is difficult to measure due to the rarity of the decay, and introducing a free parameter for it may mask potential signals in the NR region. On the other hand, the XENONnT collaboration did not incorporate this interpretation into their main result because their dataset failed to reject the model with a nominal DEC charge yield [6].

In this Letter, we provide the first combined analysis of the high-energy nuclear-recoil events in XENONnT and LZ, demonstrating that standard elastic spin-independent WIMP scattering cannot account for the observed excess, while specific velocity-dependent and inelastic scenarios can. At the same time, we identify the poorly known charge yields of ^{124}Xe double electron capture as the dominant systematic controlling the apparent preference for DM signals, and suggest XENONnT and LZ to analyze data in higher energy range to distinguish a potential DM signal from the DEC background.

Velocity-dependent and inelastic interactions.

Motivated by the excess and the insufficient understanding of the DEC charge yield, we investigate DM interpretations of the XENONnT and LZ data. Since the excess in both experiments are above $20 \text{ keV}_{\text{NR}}$, in this work,

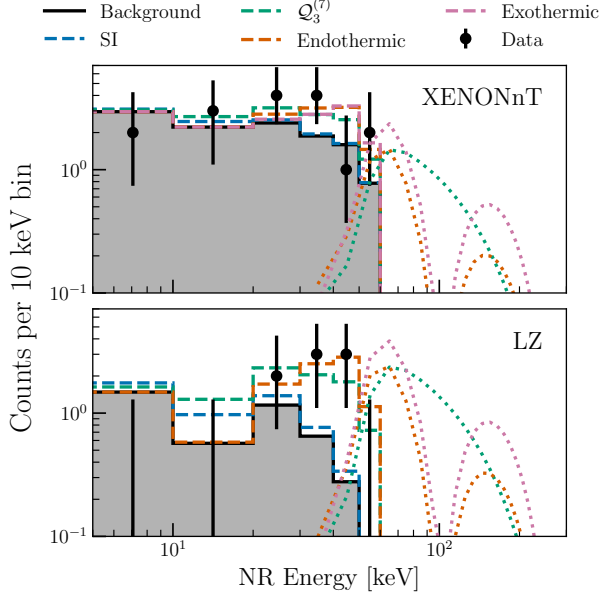


FIG. 1. Event distributions in nuclear recoil energy for XENONnT (top) and LZ (bottom). Data points are selected below or at the NR median and above the 2σ lower bound of the NR band in corrected (S1, S2); for XENONnT we additionally require $\text{cS2} > 400$ PE to mitigate low-energy mismodeling. Error bars show 1σ Feldman–Cousins intervals for signal+background counts. The black solid curve and the gray band give the predicted background under the same selection criteria, while the colored dashed curves show background plus signal for three DM benchmarks: SI scattering with $m_\chi = 200$ GeV (fixed to the 90% C.L. LZ 2024 upper limit), $\mathcal{Q}_3^{(7)}$ with $m_\chi = 100$ GeV, endothermic inelastic scattering with $\delta = 150$ keV and $m_\chi = 1$ TeV, and exothermic inelastic scattering with $\delta = -200$ keV and $m_\chi = 1$ TeV, the latter three evaluated at their combined XENONnT–LZ best-fit normalizations. Dotted lines show the predicted number of events outside the WIMP search region of interest (ROI), using the same normalization and extrapolated efficiencies but omitting the NR-band selections.

we consider two classes of DM models: The first class involves velocity-dependent DM-nucleus elastic interactions, systematically described within the DM Effective Field Theory (DMEFT) [9–17]. Two representative dimension seven operators entering our analysis are

$$\begin{aligned}\mathcal{Q}_3^{(7)} &= \frac{1}{\Lambda^3} \frac{\alpha_s}{8\pi} (\bar{\chi}\chi) G^{a\mu\nu} \tilde{G}_{\mu\nu}^a, \\ \mathcal{Q}_4^{(7)} &= \frac{1}{\Lambda^3} \frac{\alpha_s}{8\pi} (\bar{\chi} i \gamma_5 \chi) G^{a\mu\nu} \tilde{G}_{\mu\nu}^a,\end{aligned}\quad (1)$$

Here, χ denotes a spin-1/2 Dirac fermion DM particle, $G_{\mu\nu}^a$ ($\tilde{G}_{\mu\nu}^a$) are the gluon field-strength tensor and its dual, and Λ denotes the cutoff scale. We focus on these two operators because, in the nonrelativistic limit, their DM–nucleus scattering amplitudes scale as q and q^2 , respectively, where q is the momentum transfer. Consequently, the corresponding recoil-energy spectra are sup-

pressed at low E_R . Other operators can exhibit similar q -scalings; however, detailed numerical studies show that they do not fit the excess as well as $\mathcal{Q}_3^{(7)}$ and $\mathcal{Q}_4^{(7)}$.

These partonic operators are matched onto their non-relativistic counterparts at leading order in chiral counting [16]. The resulting scattering cross sections are formulated in terms of nuclear response functions, which are primarily obtained from theoretical nuclear-structure calculations and partially validated against experimental data [12]. The matching of the partonic DMEFT operators to the nonrelativistic EFT is done by a Mathematica package `DirectDM` [18]. Then, the recoil rate spectra are calculated by `DMFormFactor` [19].

The second class corresponds to inelastic DM. In this class, the DM particle transitions to a slightly heavier or lighter state with a small mass splitting, $m'_{\text{DM}} = m_{\text{DM}} + \delta$, after scattering with a nucleon. Both endothermic ($\delta > 0$) [20] and exothermic ($\delta < 0$) [21, 22] scenarios are considered. In order to isolate the effect of inelastic scattering, we focus on the vector-vector spin-independent (SI) interaction $\frac{1}{\Lambda^2} (\bar{\chi} \gamma_\mu \chi') (\bar{q} \gamma^\mu q)$. In the endothermic case, the minimum velocity required to produce a given recoil energy E_R is

$$v_{\min}(E_R) = \frac{1}{\sqrt{2m_N E_R}} \left| \frac{m_N E_R}{\mu_N} + \delta \right|, \quad (2)$$

where μ_N is the reduced DM-nuclei mass. The recoil spectra are computed following the same procedure as in the first class, and the rate spectra are obtained using the identical tool chain.

Data analysis. We incorporate full signal and background models for XENONnT and LZ into our statistical inference. In both experiments, particle interactions in LXe produce scintillation photons and ionization electrons, which generate the prompt S1 and delayed S2 signals, respectively. Each event is represented in the 2D plane of corrected S1 and S2, where the corrections remove spatial and temporal dependencies. XENONnT reports (cS1, cS2) in photoelectrons (PE), while LZ uses (S1c, S2c) in photons detected (phd). Backgrounds in both experiments fall into three broad categories: ER backgrounds, dominated by β decays of ^{214}Pb in the ^{222}Rn chain and characterized by higher S2/S1 than NR events; NR backgrounds from radiogenic neutrons and $\text{CE}\nu\text{NS}$; and data-driven backgrounds, including accidental coincidences (AC) in both experiments and surface events in XENONnT.

We use our `DIAMX` framework [23] to model the event distributions of each background and signal component in corrected S1–S2 space. `DIAMX` relies only on publicly available information and is designed to reproduce the official collaboration models as closely as possible. For simplicity, we omit $\text{CE}\nu\text{NS}$ in both experiments, neutrons in LZ, and surface events in XENONnT SR1, as their contributions are negligible. The position- and time-dependent

correction maps are not public and not included in our analysis.

The ER and NR modeling for XENONnT is based on the software **Appletree** [24]. The microphysics (NEST) parameters, describing the light and charge yields of xenon, are taken from Ref. [25] for both SR0 and SR1, and the detector parameters follow Refs. [5, 6], except that the electron gain g_2 in SR1 is adjusted to 15.8 PE/e⁻ (instead of the published (16.9 ± 0.5) PE/e⁻), likely due to small differences in the NEST parameterization between the science runs. An additional S1 reconstruction efficiency correction is applied to the XENONnT efficiency following Ref. [26]. For LZ, the ER and NR models are based on a customized version of *NEST v2.4.0* [27, 28], with parameters taken from the publicly released configuration files [3, 4]; the published ER and NR efficiencies are used directly. Data-driven backgrounds are more challenging to model due to limited public information. We assume a Gaussian-like profile for the AC background and a piecewise uniform profile for the surface background, with parameters chosen such that the published 68% and 95% contours are exactly reproduced.

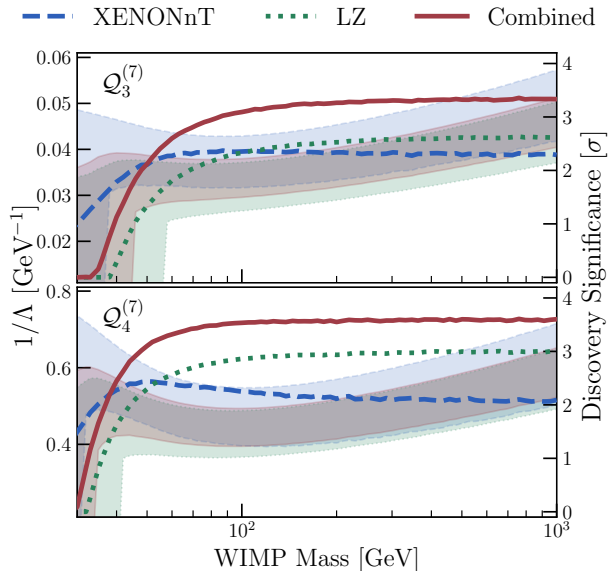


FIG. 2. Allowed 90% C.L. regions for the cutoff scale Λ (shaded bands, left y -axis) and local signal significance (lines, right y -axis) as functions of the DM mass for the DMEFT operators $Q_3^{(7)}$ and $Q_4^{(7)}$.

The event distributions generated by DIAMX agree well with the published background contours, except for NR at low energies in XENONnT. We therefore impose an additional selection $cS2 > 400$ PE on all XENONnT datasets, which also reduces the impact of surface and AC events, without affecting the high-energy excess region.

The decomposition of background components, along with their rates and associated uncertainties, follows

the corresponding publications. The neutron-recoil spectrum for XENONnT is taken from Ref. [29]. Most β decays are modeled with uniform spectra, except for ^{14}C and tritium, which follow the *BetaShape*-calculated spectrum [30] and the spectral model of Ref. [31], respectively. The ^{136}Xe two-neutrino double-beta decay spectrum follows Ref. [32].

XELDA has shown that L-shell electron-capture (EC) events of ^{127}Xe have a smaller charge yield than standard β decays [33], suggesting a similar effect for the LM- and LL-shell DEC events of ^{124}Xe . In DIAMX, we model this by introducing shape parameters $Q_X/Q_\beta \leq 1$ ($X = L, LM, LL$), defined as the ratio of the charge yield of an X -shell EC or DEC event to that of a β decay with the same energy. This treatment follows the approach adopted by the LZ collaboration [4].

To quantify the impact of uncertainties in the DEC charge yields, we evaluate all candidate DM models under three charge yield assumptions (Case I: $Q_{LM,LL}/Q_\beta = 1.0$ for XENONnT and 0.88 for LZ; Case II: Q_{LL} for LZ is floated; Case III: both Q_{LM} and Q_{LL} for XENONnT are also floated), summarized in Table I. As discussed above, the L-shell EC charge yields have been measured by LZ [34], whereas the XENONnT dataset remains compatible with a model that uses the β charge yield [6]. We therefore take Case I as our baseline. Unless otherwise stated, all results quoted below refer to this baseline.

An illustrative comparison of the observed events in corrected (S1, S2) space with the expected backgrounds and a representative endothermic inelastic DM benchmark is shown in Fig. 5 in the End Matter. We define the WIMP search ROI in corrected (S1, S2) as follows: for XENONnT, $0 < cS1 < 100$ PE and $10^{2.1} < cS2 < 10^{4.1}$ PE; for LZ WS2022 (WS2024), $3 < S1c < 80$ phd and 600 (645) $< S2c < 10^{4.5}$ phd. We refer to events with both corrected S1 and S2 above these WIMP-ROI bounds as “outside the ROI.”

DM interpretation. We perform a combined profile-likelihood analysis for each DM model. For each dataset, the likelihood includes event distributions in corrected (S1, S2) space and Gaussian constraints on the background rates; the combined likelihood is the product of the individual dataset likelihoods. Discovery significances and confidence intervals are computed using the asymptotic formulae of Ref. [35]. As a validation, we reproduce the official SI WIMP cross-section upper limits to within 10% for XENONnT SR0, XENONnT SR0+SR1, and LZ WS2022, while for LZ WS2024 our limit is weaker by $\sim 20\%$, which we attribute to the absence of radon-tagging modeling. This level of agreement confirms that our inference procedure is reliable for reinterpreting the high-energy NR excess.

For the operators $Q_3^{(7)}$ and $Q_4^{(7)}$, the Case I combined-fit results are shown in Fig. 2, with maximal local significances of about 3.3σ and 3.6σ , respectively. For both

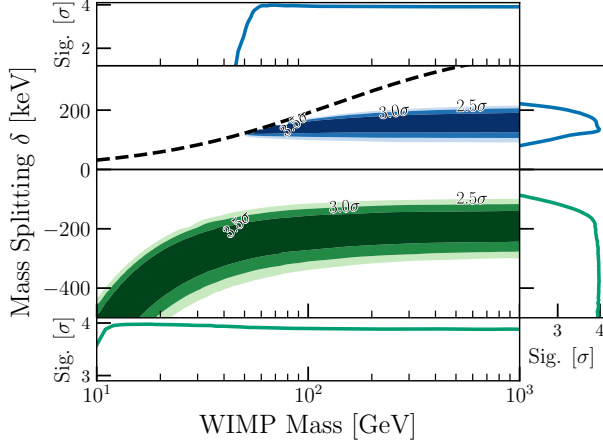


FIG. 3. Contours of the local signal significance for endothermic (blue) and exothermic (green) inelastic DM in the (m_{DM}, δ) space. The black dashed line marks the kinematic threshold below which endothermic scattering in xenon is kinematically forbidden. The panels on the sides show the marginalized local significances as functions of m_{DM} and δ .

operators, the preferred cutoff scale Λ lies in the range $\mathcal{O}(1 - 10)$ GeV, indicating that the interactions are mediated by light states. The significance contours for inelastic DM are shown in Fig. 3. In the endothermic case, we find local significances above 3σ for mass splittings $\delta \simeq 110\text{--}205$ keV. In this regime, only DM particles with velocities above the kinematic threshold in Eq. 2 can scatter, naturally concentrating the signal at higher recoil energies while strongly suppressing the rate at lower energies. For exothermic scattering, we obtain local significances up to 3σ for $\delta < -105$ keV. The characteristic recoil energy is set by the point where $v_{\text{min}} = 0$, $E_R^* \equiv |\delta| \frac{m_{\text{DM}}}{m_{\text{DM}} + m_N}$, which naturally populates the observed high-recoil excess while suppressing low-energy events in xenon over the preferred parameter region. The scaling of E_R^* also explains the 3σ band in Fig. 3: as m_{DM} decreases, a larger $|\delta|$ is required to keep E_R^* fixed. Thus, both endothermic and exothermic inelastic scattering can account for the observed high-energy nuclear-recoil excess without overproducing low-energy events.

Using a set of representative benchmarks, we also predict the event rate at higher NR energies. In Fig. 4, we show four DM benchmarks as functions of m_{DM} , with the predicted numbers of events inside (dashed) and outside (solid) the ROI. For the two velocity-dependent benchmarks, the out-of-ROI yield exceeds $\mathcal{O}(30)$ events at large m_{DM} . The event yield from $Q_7^{(4)}$ is significantly larger than that from $Q_7^{(3)}$, owing to their different q -scaling. Since the LZ data at higher NR energy show no corresponding large excess under a nominal background model [36, 37], we infer $m_{\text{DM}} \lesssim 110$ GeV and 70 GeV for $Q_7^{(3)}$ and $Q_7^{(4)}$, respectively. Complementary information

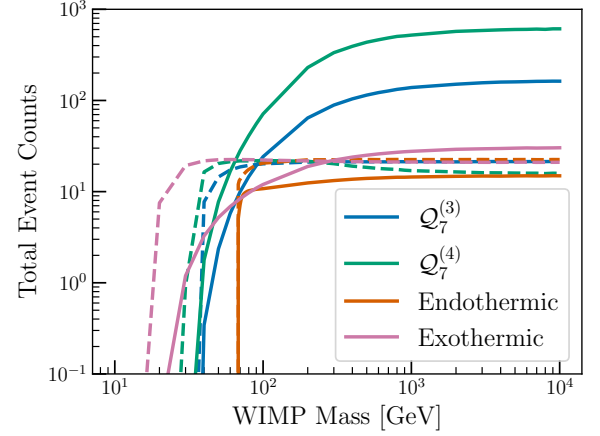


FIG. 4. Predicted total number of events inside (dashed) and outside (solid) the WIMP search ROI for the four DM benchmarks, assuming the exposure of the 7.3 tonne \times year of XENONnT and LZ. The models include $Q_7^{(3)}$, $Q_7^{(4)}$, endothermic inelastic scattering with $\delta = 150$ keV, and exothermic inelastic scattering with $\delta = -200$ keV. All four are evaluated at their combined XENONnT –LZ best-fit normalizations.

is provided by Fig. 1, which shows the NR spectra of out-of-ROI events for the $Q_7^{(3)}$ and exothermic/endothermic benchmarks. The spectra peak in the range 50–200 keV, indicating where the predicted out-of-ROI events are concentrated.

For inelastic DM, we take $\delta = -200$ and 150 keV for exothermic and endothermic scattering. In the endothermic case, the out-of-ROI rate turns on around $m_{\text{DM}} \sim 70$ GeV sharply and saturates at ~ 10 events for $m_{\text{DM}} \gtrsim 500$ GeV, while in the exothermic case it grows to ~ 30 events at TeV-scale masses and then levels off. In both inelastic benchmarks, the predicted high-recoil yield is at the level of a few tens of events, providing a clear target for upcoming analysis of XENONnT and LZ data.

Finally, we assess the robustness of these conclusions under different DEC charge-yield assumptions. As shown in Table I, the formal local significances for our benchmark DM models are sensitive to this choice: they can exceed 4σ in our baseline assumption (Case I), but fall below 1.6σ for all models in the most conservative case (Case III). This spread shows that current DEC systematics dominate the quantitative significance, even though the qualitative preference for spectra that enhance high energy NR events remains.

Discussions and Conclusions. We investigate DM interpretations of the high-energy NR excess reported by recent liquid-xenon experiments. Using our unified DIAMX framework, built on publicly available data and likelihood models, we perform the first combined profile-likelihood fits across multiple WIMP-search datasets, totaling 7.3 tonne \times year of exposure. We show that

two broad classes of DM–nucleon interactions—velocity-dependent cross sections and inelastic scattering (both endo- and exothermic)—can reproduce the observed high-energy NR spectrum, yielding local significances up to 4σ . We quantify the impact of the ^{124}Xe DEC background, finding that plausible variations in the poorly known DEC charge yield can shift the inferred local significance for DM models down to below 1σ .

Within DMEFT, the velocity-dependent operators $\mathcal{Q}_3^{(7)}$ and $\mathcal{Q}_4^{(7)}$ can accommodate the excess at the few- σ level. The best-fit values imply cutoff scales of $\mathcal{O}(1-10)$ GeV as shown in Fig. 2. When combined with collider searches [38, 39], this suggests that if these interactions are responsible for the excess, the DM-gluon coupling must be mediated by light states. For endothermic and exothermic inelastic DM scenarios, the cutoff scale Λ is $\mathcal{O}(10)$ TeV (see End Matter), safely evading collider bounds.

Using the best-fit benchmarks, we also predict the event rate at higher NR energies outside the present ROI. Velocity-dependent models tend to overproduce such events at large m_{DM} , while inelastic benchmarks robustly forecast only a few tens of high-recoil events. Improved measurements of DEC charge yields, together with extended high-recoil searches in upcoming analysis of XENONnT and LZ data, will therefore be crucial to determining whether the excess is due to DM or to previously unmodeled backgrounds.

Acknowledgements. The work of H.A., H.N. and C.X. is supported in part by the National Key R&D Program of China under Grant Nos. 2023YFA1607104 and 2021YFC2203100 and the National Science Foundation of China under Grant Nos. 12475107 and 12525506. The work of F.G. and M.L. is supported by the National Science Foundation of China under Grant No. 12521007. H.A. and F.G. acknowledge support from the Dushi program of Tsinghua University and the Tsinghua University Initiative Scientific Research Program. The work of J.L. is supported by NSFC (Nos. 12235001, 12475103) and State Key Laboratory of Nuclear Physics and Technology under Grant No. NPT2025ZX11.

* anhp@tsinghua.edu.cn

† feigao@tsinghua.edu.cn

‡ jialiu@pku.edu.cn

§ ml5107@columbia.edu

¶ nhm20@mails.tsinghua.edu.cn

** xuchanglong@mail.tsinghua.edu.cn

- [1] P. Hut, Limits on masses and number of neutral weakly interacting particles, *Phys. Lett. B* **69**, 85 (1977).
- [2] B. W. Lee and S. Weinberg, Cosmological lower bound on heavy-neutrino masses, *Phys. Rev. Lett.* **39**, 165 (1977).
- [3] J. Aalbers *et al.* (LZ Collaboration), First Dark Matter Search Results from the LUX-ZEPLIN (LZ) Experiment, *Phys. Rev. Lett.* **131**, 041002 (2023), arXiv:2207.03764 [hep-ex].
- [4] J. Aalbers *et al.* (LZ Collaboration), Dark Matter Search Results from 4.2 Tonne-Years of Exposure of the LUX-ZEPLIN (LZ) Experiment, *Phys. Rev. Lett.* **135**, 011802 (2025), arXiv:2410.17036 [hep-ex].
- [5] E. Aprile *et al.* (XENON Collaboration), First Dark Matter Search with Nuclear Recoils from the XENONnT Experiment, *Phys. Rev. Lett.* **131**, 041003 (2023), arXiv:2303.14729 [hep-ex].
- [6] E. Aprile *et al.* (XENON Collaboration), WIMP Dark Matter Search Using a 3.1 Tonne-Year Exposure of the XENONnT Experiment, *Phys. Rev. Lett.* **135**, 221003 (2025), arXiv:2502.18005 [hep-ex].
- [7] Z. Bo *et al.* (PandaX Collaboration), Dark Matter Search Results from 1.54 Tonne-Year Exposure of PandaX-4T, *Phys. Rev. Lett.* **134**, 011805 (2025), arXiv:2408.00664 [hep-ex].
- [8] E. Aprile *et al.* (XENON Collaboration), Dark matter search results from a one ton-year exposure of XENON1T, *Phys. Rev. Lett.* **121**, 111302 (2018).
- [9] Q.-H. Cao, C.-R. Chen, C. S. Li, and H. Zhang, Effective Dark Matter Model: Relic density, CDMS II, Fermi LAT and LHC, *JHEP* **08**, 018, arXiv:0912.4511 [hep-ph].
- [10] H. An, S.-L. Chen, R. N. Mohapatra, S. Nussinov, and Y. Zhang, Energy Dependence of Direct Detection Cross Section for Asymmetric Mirror Dark Matter, *Phys. Rev. D* **82**, 023533 (2010), arXiv:1004.3296 [hep-ph].
- [11] J. Fan, M. Reece, and L.-T. Wang, Non-relativistic effective theory of dark matter direct detection, *JCAP* **11**, 042, arXiv:1008.1591 [hep-ph].
- [12] A. L. Fitzpatrick, W. Haxton, E. Katz, N. Lubbers, and Y. Xu, The Effective Field Theory of Dark Matter Direct Detection, *JCAP* **02**, 004, arXiv:1203.3542 [hep-ph].
- [13] V. Gluscevic, M. I. Gresham, S. D. McDermott, A. H. G. Peter, and K. M. Zurek, Identifying the Theory of Dark Matter with Direct Detection, *JCAP* **12**, 057, arXiv:1506.04454 [hep-ph].
- [14] A. De Simone and T. Jacques, Simplified models vs. effective field theory approaches in dark matter searches, *Eur. Phys. J. C* **76**, 367 (2016), arXiv:1603.08002 [hep-ph].
- [15] S. Liem, G. Bertone, F. Calore, R. Ruiz de Austri, T. M. P. Tait, R. Trotta, and C. Weniger, Effective field theory of dark matter: a global analysis, *JHEP* **09**, 077, arXiv:1603.05994 [hep-ph].
- [16] F. Bishara, J. Brod, B. Grinstein, and J. Zupan, From quarks to nucleons in dark matter direct detection, *JHEP* **11**, 059, arXiv:1707.06998 [hep-ph].
- [17] H. Song, H. Sun, and J.-H. Yu, Complete EFT operator bases for dark matter and weakly-interacting light particle, *JHEP* **05**, 103, arXiv:2306.05999 [hep-ph].
- [18] F. Bishara, J. Brod, B. Grinstein, and J. Zupan, DirectDM: a tool for dark matter direct detection (2017), arXiv:1708.02678 [hep-ph].
- [19] N. Anand, A. L. Fitzpatrick, and W. C. Haxton, Weakly interacting massive particle-nucleus elastic scattering response, *Phys. Rev. C* **89**, 10.1103/physrevc.89.065501 (2014).
- [20] D. Tucker-Smith and N. Weiner, Inelastic dark matter, *Phys. Rev. D* **64**, 043502 (2001), arXiv:hep-ph/0101138.
- [21] P. W. Graham, R. Harnik, S. Rajendran, and P. Saraswat, Exothermic Dark Matter, *Phys. Rev. D* **82**, 063512 (2010), arXiv:1004.0937 [hep-ph].
- [22] B. Batell, M. Pospelov, and A. Ritz, Direct Detection

- of Multi-component Secluded WIMPs, *Phys. Rev. D* **79**, 115019 (2009), arXiv:0903.3396 [hep-ph].
- [23] M. Liu, mliu0001/diamx: v0.2.0 (2025).
 - [24] D. Xu, Z. Xu, M. Liu, Y. Ma, J. R. Angevaare, L. Yuan, and L. Hoetsch, XENONnT/appletree: v0.5.4 (2025).
 - [25] E. Aprile *et al.* (XENON Collaboration), XENONnT WIMP search: Signal and background modeling and statistical inference, *Phys. Rev. D* **111**, 103040 (2025), arXiv:2406.13638 [physics.data-an].
 - [26] E. Aprile *et al.* (XENON Collaboration), XENONnT analysis: Signal reconstruction, calibration, and event selection, *Phys. Rev. D* **111**, 062006 (2025), arXiv:2409.08778 [hep-ex].
 - [27] M. Szydagis, N. Barry, K. Kazkaz, J. Mock, D. Stolp, M. Sweany, M. Tripathi, S. Uvarov, N. Walsh, and M. Woods, NEST: A Comprehensive Model for Scintillation Yield in Liquid Xenon, *JINST* **6**, P10002, arXiv:1106.1613 [physics.ins-det].
 - [28] M. Szydagis *et al.*, A review of NEST models for liquid xenon and an exhaustive comparison with other approaches, *Front. Detect. Sci. Tech.* **2**, 1480975 (2024), arXiv:2211.10726 [hep-ex].
 - [29] E. Aprile *et al.* (XENON Collaboration), Projected WIMP sensitivity of the XENONnT dark matter experiment, *JCAP* **11**, 031, arXiv:2007.08796 [physics.ins-det].
 - [30] X. Mougeot, Atomic exchange correction in forbidden unique beta transitions, *Applied Radiation and Isotopes* **201**, 111018 (2023).
 - [31] M. Kleesiek *et al.*, β -Decay Spectrum, Response Function and Statistical Model for Neutrino Mass Measurements with the KATRIN Experiment, *Eur. Phys. J. C* **79**, 204 (2019), arXiv:1806.00369 [physics.data-an].
 - [32] J. Kotila and F. Iachello, Phase-space factors for double- β decay, *Phys. Rev. C* **85**, 034316 (2012).
 - [33] D. J. Temples, J. McLaughlin, J. Bargemann, D. Baxter, A. Cottle, C. E. Dahl, W. H. Lippincott, A. Monte, and J. Phelan, Measurement of charge and light yields for Xe127 L-shell electron captures in liquid xenon, *Phys. Rev. D* **104**, 112001 (2021), arXiv:2109.11487 [physics.ins-det].
 - [34] J. Aalbers *et al.* (LZ Collaboration), Measurements and models of enhanced recombination following inner-shell vacancies in liquid xenon, *Phys. Rev. D* **112**, 012024 (2025), arXiv:2503.05679 [hep-ex].
 - [35] G. Cowan, K. Cranmer, E. Gross, and O. Vitells, Asymptotic formulae for likelihood-based tests of new physics, *Eur. Phys. J. C* **71**, 1554 (2011), [Erratum: *Eur. Phys. J. C* **73**, 2501 (2013)], arXiv:1007.1727 [physics.data-an].
 - [36] J. Aalbers *et al.* (LZ), First constraints on WIMP-nucleon effective field theory couplings in an extended energy region from LUX-ZEPLIN, *Phys. Rev. D* **109**, 092003 (2024), arXiv:2312.02030 [hep-ex].
 - [37] J. Aalbers *et al.* (LZ), Constraints on Covariant Dark-Matter–Nucleon Effective Field Theory Interactions from the First Science Run of the LUX-ZEPLIN Experiment, *Phys. Rev. Lett.* **133**, 221801 (2024), arXiv:2404.17666 [hep-ex].
 - [38] J. Goodman, M. Ibe, A. Rajaraman, W. Shepherd, T. M. P. Tait, and H.-B. Yu, Constraints on Dark Matter from Colliders, *Phys. Rev. D* **82**, 116010 (2010), arXiv:1008.1783 [hep-ph].
 - [39] H. An, X. Ji, and L.-T. Wang, Light Dark Matter and Z' Dark Force at Colliders, *JHEP* **07**, 182, arXiv:1202.2894 [hep-ph].

End Matter

Figure 5 shows the corrected (S1, S2) distributions for all XENONnT and LZ datasets, visualized event-by-event as pie charts that encode the relative contributions of background and representative endothermic inelastic DM benchmarks, using the best-fit parameters from Cases I and II. This illustrates how the high-recoil excess can be attributed predominantly to the DM component while remaining consistent with the lack of a low-energy excess. Table I summarizes the DEC charge-yield assumptions (Cases I–III) and the corresponding maximal local significances and best-fit parameters for our benchmark DM models.

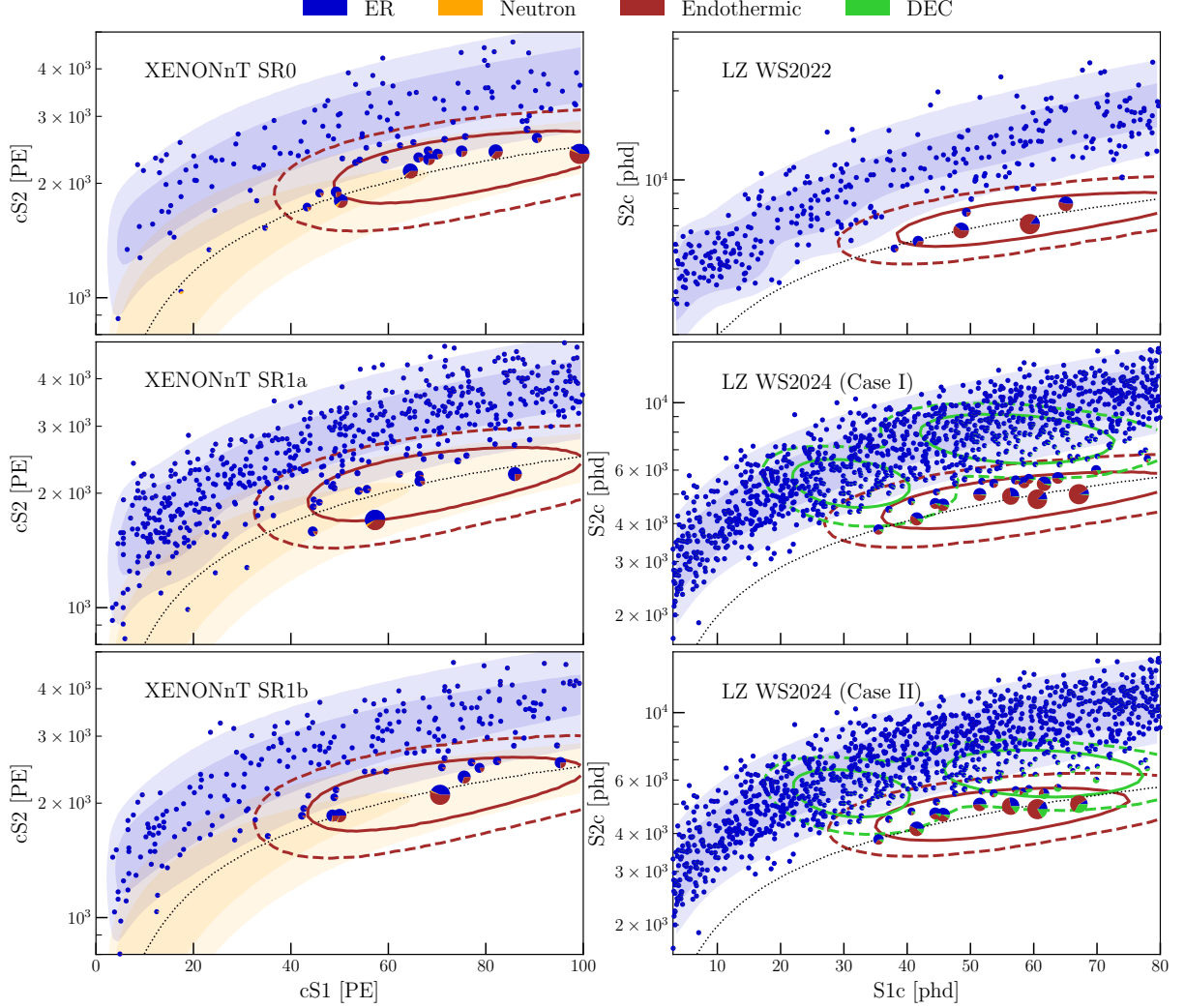


FIG. 5. Corrected (S1, S2) distributions for all XENONnT and LZ datasets used in this analysis. Each event is represented by a pie chart showing the fractional contributions of the local probability density from different components of the best-fit endothermic inelastic DM model. In the 3×2 panel layout, the first five panels (the top two rows and the lower-left panel) use the best-fit benchmark ($\delta = 135$ keV, $m = 70$ GeV) under the baseline DEC charge-yield treatment (Case I), while the lower-right panel uses the Case II best-fit benchmark ($\delta = 130$ keV, $m = 60$ GeV). The pie size is proportional to the local endothermic signal fraction. Shaded regions indicate the 1σ and 2σ contours for ER (blue) and neutron (orange) backgrounds. Solid and dashed curves show the corresponding contours for the endothermic signal (red) and the ¹²⁴Xe background (green), respectively.

TABLE I. Ratios of Q_L , Q_{LM} , and Q_{LL} to Q_β for the different DEC charge-yield scenarios and datasets. The label *float* indicates that the ratio is treated as an independent free parameter in the combined fit. The last two columns show the maximum local signal significance and the corresponding best-fit parameters for each scenario.

Case	Experiment	Q_{LM}/Q_β	Q_{LL}/Q_β	Model	Sig.	Best-fit Para. (Λ , m_χ , $ \delta $)
I	XENONnT	1.00	1.00	$Q_3^{(7)}$:	3.3σ	(22.0 GeV, 832 GeV, -)
				$Q_4^{(7)}$:	3.6σ	(1.75 GeV, 759 GeV, -)
	LZ	0.88	0.88	Endothermic:	4.0σ	(5.04 TeV, 70 GeV, 135 keV)
				Exothermic:	4.0σ	(80.9 TeV, 19 GeV, 350 keV)
II	XENONnT	1.00	1.00	$Q_3^{(7)}$:	1.3σ	(24.8 GeV, 759 GeV, -)
				$Q_4^{(7)}$:	1.3σ	(2.29 GeV, 219 GeV, -)
	LZ	0.88	<i>float</i>	Endothermic:	2.3σ	(3.16 TeV, 60 GeV, 130 keV)
				Exothermic:	2.3σ	(95.9 TeV, 14 GeV, 410 keV)
III	XENONnT	<i>float</i>	<i>float</i>	$Q_3^{(7)}$:	0.2σ	(32.4 GeV, 955 GeV, -)
				$Q_4^{(7)}$:	0.5σ	(2.69 GeV, 251 GeV, -)
	LZ	0.88	<i>float</i>	Endothermic:	1.6σ	(3.42 TeV, 60 GeV, 130 keV)
				Exothermic:	1.7σ	(~ 100 TeV, ~ 10 GeV, >500 keV)